Persistent pitch angle anisotropies of relativistic electrons in the outer radiation belts

A.D. Greeley[1], S.G. Kanekal[1], Q. Schiller[2], L. Blum[3], A. Halford[1], K. Murphy[4,5], T. Raita[6], D.N. Baker[3]

[1]NASA Goddard Space Flight Center, Greenbelt, MD, United States
[2]George Mason University, Fairfax, VA, United States
[3]Laboratory for Atmospheric and Space Physics, Univeristy of Colorado, Boulder, CO, United States
[4]Independent Researcher, Thunder Bay, ON, Canada
[5]Department of Maths, Physics and Electrical Engineering, Northumbria University, Newcastle Upon Tyne, United Kingdom
[6]Sodankylä Geophysical Observatory, University of Oulu, Finland

Key Points:

- Persistent pitch angle distribution anisotropy is observed over two days associated with EMIC waves
- EMIC waves during geomagnetically quiet periods can have long lasting effect on radiation belts
- Multipoint measurements can help pinpoint important mechanisms in radiation belt dynamics

Corresponding author: A. Greeley, `ashley.greeley@nasa.gov`

Abstract

Pitch Angle Distributions in the radiation belts are well characterized with $sin^n(\alpha)$. By tracking the exponent 'n', termed Pitch Angle Index, we are able to observe persistent and cross energy changes in pitch angle distributions of Van Allen radiation belt electrons using Van Allen Probes particle observations. The pitch angle distributions measurements are well fit down to a single satellite spin, and therefore can track spatially and temporally confined changes to determine connection between particles and waves. We use the Van Allen Probes data in conjunction with Geostationary Operational Environmental Satellites (GOES) spacecraft and several ground magnetometer stations from Canadian Array for Realtime Investigations of Magnetic Activity (CARISMA) and Finnish pulsation magnetometer network of Sodankylä Geophysical Observatory (SGO) to connect particles that become very anisotropic to electromagnetic ion cyclotron (EMIC) waves during a quiet period over two days, June 26 and 27, 2013. The waves and peaks in the particle PADs are both long lasting but spatially separated, suggesting that wave particle interactions in the inner magnetosphere can occur for extend periods of time and have significant impact on the global radiation belts, even during otherwise geomagnetically quiet times and when wave activity is highly localized.

Plain Language Summary

The Van Allen Radiation belts can trap energetic electrons in the magnetic fields surrounding Earth. Often, these particles are studied during time periods of strong geomagnetic activity. However, quiet times can also result in interesting distributions and interactions in the radiation belts. We study one such geomagnetically quiet time where electron pitch angle distributions are suddenly and persistently anisotropic, as observed by instruments on the Van Allen Probes twin satellites. Neither probes observes electromagnetic waves that could cause anisotropic pitch angle distributions, but other satellites and ground measurements indicated wave activity during this time period. In both cases, the waves and peaks in the particle pitch angle distributions are long lasting. This suggests that wave particle interactions in the inner magnetosphere can occur for extend periods of time and have significant impact on the global radiation belts, even during otherwise geomagnetically quiet times and when wave activity is highly localized.

1 Introduction

Physical processes contributing to electron dynamics (S. Kanekal & Miyoshi, 2021) in the Earth's radiation belts, particularly the outer zone, are well characterized by direct measurements of electron spectra, pitch angle distributions (PADs), and the temporal evolution thereof. Early observations of the temporal evolution of electron spectra from the SAMPEX (Solar Anomalous Magnetospheric Particle Explorer) spacecraft helped establish connection between substorm injected seed population and their subsequent energization to relativistic energies (Baker et al., 1998). Around the same time period, measurements from NASA's Polar satellites showed relativistic electron acceleration occurring on the scale of ∼12 hours, much more rapidly than previously thought (Reeves et al., 1998). About a decade later, a study utilizing data from SAMPEX in LEO and Polar at high altitudes examined the connection between electron energization and pitch angle distribution isotropization (S. G. Kanekal et al., 2005). More recently, A. D. Greeley et al. (2019) studied PAD evolution of relativistic and ultra relativistic electron enhancements during CIR- and CME-driven storms and showed that outer zone electron populations exhibited strong anisotropy (peaked $\sim 90^\circ$) soon after storm main phase with driver-dependent relaxation times. They found that, during storms, relatively higher energy electrons had higher anisotropies than lower energy electrons (within the >1 MeV populations). Changes in the PADs leading to either narrowing of pitch angle distributions or isotropization occurs as a result of wave-particle interactions, i.e, these interactions scatter electrons and dynamically alter electron PADs (for a recent review see (Baker, 2021). Wave-particle interactions involve a variety of plasma waves in the magnetosphere including whistler-mode chorus, plasmaspheric hiss, EMIC, and ULF waves that can interact with charged particles in either a resonant, stochastic, or non-linear manner (Thorne et al., 2021; Blum & Breneman, 2020).

It is currently understood that observed electron fluxes in the outer zone are the result of two competing processes, namely energization and loss (Reeves et al., 2013). Wave-particle interactions have long been invoked to explain the both energization and loss of outer zone electrons and the cause of the slot region (Thorne, 2010; Abel & Thorne, 1998). More recently, direct observation of wave particle interactions (Fennell et al., 2014; Kasahara et al., 2018) were able to measure concomitant changes in PADs with wave activity utilizing high-fidelity observations from improved instruments.

Waves that scatter electrons into the loss cone resulting in their removal from the outer zone include plasmaspheric hiss, whistler mode chorus, as well as EMIC waves. At high L-shells ($L \approx 5.$) and for relativistic electrons, it is the latter that is the most relevant scattering mechanism; chorus are less efficient at precipitating high energy electrons near the loss cone by resonant interactions (Horne & Thorne, 2003). Although plasmaspheric hiss is a contender due to the presence of plumes which can extend into higher L shells, the associated lifetimes tend to be of the order several days, e.g. > 100 days for 5 MeV electrons (Ni et al., 2013) associated with resonant interactions. A study by Claudepierre et al. (2020) compared observed decay time scales with models that distinguished contributions by specific wave types, strongly suggesting that EMIC waves were predominantly responsible for scattering relativistic electrons. A statistical study using 4 years of Van Allen Probes data showed that relativistic electron interactions with EMIC wave led to narrowing of PAD during geomagnetically active periods (Zhao et al., 2019). Further compelling evidence for EMIC wave causing relativistic electron precipitation comes from event studies showing simultaneous EMIC wave and electron precipitation (Blum et al., 2015; Usanova et al., 2014; Zhang et al., 2016; Bingley et al., 2019; Medeiros et al., 2019; Nakamura et al., 2022). Detailed simulations of non-linear interactions involving EMIC waves have suggested that the time scales involved in scattering relativistic and ultra-relativistic particle are quite rapid, on the order of minutes (Kubota & Omura, 2017).

In this paper, we report on in-situ observations of relativistic electron PAD at high L-shells (≈ 5) made by instruments onboard the Van Allen Probes. Our observations show a sudden and sharp narrowing of pitch angle distributions. The narrowing of PADs persist for many orbits and are confined to a small spatial extent around ≈ 5 in L. We combine the particle observations with ground-based measurements of EMIC waves and examine their possible causal association. This paper is organized as follows: Section 2 describes data and our analysis methods, Section 3 describes particle and wave observations, Section 4 provides a discussion and interpretation of our findings, and lastly, Section 5 summarizes our results.

2 Data and Methods

2.1 Spacecraft and Ground magnetometers

This study utilizes comprehensive multi-point measurements of particle and wave data from the Van Allen Probes, CARISMA (Canadian Array for Realtime Investigations of Magnetic Activity) array, Finnish pulsation magnetometer network of Sodankylä Geophysical Observatory (SGO) ground stations, and GOES (Geostationary Operational Environmental Satellites) 13 and 15. Van Allen Probes provide particle and wave observations, and GOES, CARISMA, and SGO supplement wave data.

The Van Allen Probes (formerly known as Radiation Storm Belt Probes, RBSP), comprise twin spacecraft (denoted hereinafter as Probes A and B) that were launched into a near-equatorial, highly elliptical orbit in late August 2012 and collected data for 7 years until decommissioning in 2019 (Mauk et al., 2013). Both probes have comprehensive identical instrument suites which characterize particles, waves, and fields in the magnetosphere. Both the probes spin at ∼6 rotations per minute (RPM) which enables the particle instruments to provide pitch angle coverage of the in-situ plasma. Each probe carries, as part of the Energetic Particle, Composition, and Thermal Plasma suite (Spence et al., 2013), the Relativistic Electron Proton Telescope (REPT) (Baker et al., 2012) and the Magnetic Electron and Ion Sensor (MagEIS) instrument (Blake et al., 2013). The REPT instrument is a solid-state detector particle telescope measuring ∼2-20 MeV electrons in 8 differential energy channels, while MagEIS consists of 3 magnetic spectrometers; low-, medium- and high-energy units, that cover a lower range of energies for electrons (∼20 keV-4 MeV). Together, the REPT and MagEIS instruments enable complete characterization of outer zone electrons from source, seed to ultra-relativistic energies (Jaynes et al., 2015). Particle measurements from REPT and MagEis have made significant and vital contributions and discoveries to radiation belt electron dynamics (Baker et al., 2021; Claudepierre et al., 2021).

The series of NASA and NOAA's Geostationary Operational Environmental Satellite (GOES) instruments have been in geosynchronous orbit since 1975. GOES satellites < 16 have fluxgate magnetometer data available at 2 Hz, which allow for some EMIC wave detection, but there are noise floor limitations. GOES satellites also have a particle suite, although this study utilizes the magnetometers only. GOES 13-15 were all in orbit in 2013, and 13 and 15 were ultimately used for this study. GOES 13 orbits at L=6.8 and GOES 15 orbits at L=6.6.

CARISMA is a network of 28 ground magnetometer stations in North America (Mann et al., 2008) that has data available from 1 Hz up to 20 Hz. The CARISMA stations include fluxgate magnetometer and induction-coil magnetometer instruments which both track magnetic field perturbations over a range of latitudes. SGO search coil magnetometers are sampled with 40Hz witd 3dB cut-off at 10Hz. Six stations had data availability in 2013, and we use the z-component of the pulsations in our analysis. Measurements at a particular latitude can be associated with an L-shell footprint by tracing the magnetic field at the location of a ground-based magnetometer to the magnetosphere thereby, connecting satellite in-situ measurements with ground-based data. Ground based geomagnetic field variations in the 0.1-4 Hz range (called Pc1-2 pulsations) have been shown to be associated with in-situ EMIC waves (Jacobs et al., 1964; Anderson et al., 1992; Usanova & Blum, 2021). While the possibility of ionospheric ducting makes it difficult to determine the source region of EMIC waves in the inner magnetosphere and outer radiation belt using ground magnetometer data, ground-based measurements still allow for the existence and duration of EMIC waves to be determined.

2.2 Method of determining Pitch Angle Index

It has long been known that electron pitch angle distributions and their evolution provide valuable insight into electron dynamics. These distributions are typically described by characteristic shapes such as butterfly, flattop, and pancake (West Jr. et al., 1973; Zhao et al., 2018). To characterize these PADs, studies have used $J_0 sin^n \alpha$ function to fit pancake and flattop pitch angle distributions (A. D. Greeley et al., 2021; Ni, Zou, et al., 2015; Gannon et al., 2007). Recently, A. D. Greeley et al. (2021) temporally averaged electron PADs from the the Van Allen Probes over several spins. These averaged PADs were then fit to $J_0 sin^n \alpha$. The fits were done for the entire outer radiation belt and were used to study the long-term evolution of relativistic and ultra-relativistic electrons PADs by investigating the temporal and spatial variation in the pitch angle index n (PAI). Here we expand upon this analysis technique to examine rapid spatial and temporal changes in electron PADs, with temporal resolution limited only by the spin rate of 11 seconds of the Van Allen Probes instead of the averaged together over many spins, as previously reported.

In our analysis, local pitch angles are translated to equatorial pitch angles using the conservation of $sin^2(\alpha)/B$, where equatorial B is modeled using OP77Q and IGRF for the external and internal fields, respectively. The equatorial pitch angle distributions (where pitch angle is between 20 and 160 degrees) are then fit with the form $sin^n(\alpha)$, where fits are restricted to RMSE less than 0.3. Butterfly PADs are generally not modeled well by the assumed functional form, although can result in 'n' values <0, depending on the depth of their trough at 90 degrees and maxima of the PADs. We remove them via the method descirbed by Zhao et al. (2019). We also restrict PADs to MLAT $< 15°$, since although assumption of isoptropy allows for a $sin^n(\theta)$ fit in many cases, knowledge of the 90° population is not possible far off the equator. A thorough description of the fitting method is outlined in (A. D. Greeley et al., 2019). Relatively higher values of PAI are considered to be more anisotropic, i.e., peaked more narrowly around 90°.

In the following sections, we analyze the evolution of PADs using the PAI over a period of two days, starting on June 26, 2013. In addition, we use electron Phase Space Densities (PSD) obtained using the full particle instrument onboard RBSP (Boyd et al., 2018), fluxgate magnetometer data from GOES 13 and 15, and ground magnetometer data from the CARISMA and SGO chains to provide a comprehensive picture of this event period.

3 Observations

On June 27, 2013, there was a sudden storm commencement (SSC), indicated by sharp changes in SymH, solar wind, proton density, and the southward component of the interplanetary magentic field Bz. However, the two days prior to this storm were fairly quiet in terms of geomagnetic indices. Prior to the SSC during the quiet period, electron PADs in the outer radiation belts as observed by REPT and MagEIS become more sharply peaked around 90° in a spatially confined region in L and over a wide range of energies (∼0.5-4.2 MeV). The anisotropy persists over time corresponding to dozens of drift periods of the electron populations. As quantified by PAI, higher values indicate relatively higher anisotropy. A PAI near 1 is isotropic (the PAD is fit well by $sin(\alpha)$), whereas a PAI near 5 is highly anisotropic (the PAD is fit well by $sin^5(\alpha)$.

Figures 1 and 2 show particle, interplanetary, and geomagnetic activity data for June 26 (Figure 1) and June 27 (Figure 2). Panels a) in both figures show particle data from Probe A, and panels b) are from Probe B. The panels show PAI as a function of time for 9 electron differential energy channels, colors indicating the energy channel. The lower four energy channels, 0.47-1.65 MeV, are from MagEIS, and the five higher energy channels, 1.8-4.2 MeV, are measured by REPT. Time in UT is shown on the x axis, along with L*, MLT, and MLAT for both spacecraft. Gaps in the particle data are due to the selection criteria for MLAT (Section 2.2). Inbound and outbound passes of the probes through the radiation belts are marked with a red dotted line with a nearby vertical label.

On both June 26 and 27, there are significant changes in PAI on the otherwise slowly varying PAI plots that are persistent in time and space. Slow variations in the PAI are common when the radiation belts are quiet and the electron populations are unchanging. The significant changes indicated are observed as very linear, large slopes that comes to a distinct peak before linearly dropping again. A gray box encompasses each of these peaks in the figures. On June 26, the sharp anisotropy change is first observed in Probe B ∼1015 UT. It is observed in the next two Probes B and A passes. On June 27, the anisotropy peaks are first observed on Probe B ∼1000 UT and its next pass, as well as a single pass on Probe A. The PAI peaks are observed clearly in channels >1 MeV in both REPT and MagEIS instruments. On June 26, the anisotropy may be observed down to 470 keV, and on June 27, the peak is observable to around 1.1 MeV. Both Probes A and B are missing PAI data points from 2100 UT on June 26 through 0600 UT on June 27. During this time period, MLAT was greater than 15 degrees, so the confidence in the fit is low and therefore not included in the plots or the subsequent analysis. Despite that, there is still an observable peak in the data, not shown, so the anisoptropy likely does persist through this time period. Panels c), d), and e) show the SymH, proton density, and magnetic field in the Z direction for both dates. The time period is relatively quiet until 1500 UT on June 27, when there is a SSC, noted by a sharp change in the SymH and proton density, and drop in Bz. The PAD anisotropy is observed before the storm commencement, when the geomagnetic are otherwise quiet.

On June 26, steepening electron anisotropy is first observed at 1015 UT on Probe B at an ∼22 MLT and 5.2 L* as the probe is traveling inbound through the outer radiation belt. Probe B continues to observe the anisotropy in its next two passes (outbound and inbound). On the outbound pass, the probe has an MLT of ∼20 and L*=5.2 while passing through the anisotropic region. Probe A, following a few hours behind Probe B, observes the anisotropy for two passes. The anisotropy is last observed at 1920 UT on Probe B on this day. The anisotropy peaks occur roughly in the same location across energy channels, although relatively lower energy electrons are most peaked at slightly higher L* than higher energy electrons (L*=5.2 for 4.2 MeV electrons vs. L*= 5.3 for 1.8 MeV electrons. The last pass in Probe A on the June 26 is not included in the study due to the off equatorial location of the probe, which limits knowledge of the 90 degree equatorial pitch angles during this pass.

On June 27, electron anisotropy is observed first in Probe B at 1020 UT at ∼20 MLT and L*=4.9 on its outbound pass. Probe A observed the anisotropy very shortly thereafter on its inbound pass (∼1030 UT, just ten minutes later). Probe B also observes the anisotropy on its next inbound pass at ∼1330 UT. There is a sudden storm commencement before Probe A's next pass (indicated by the sudden changes in SymH, proton density, and Bz), and the PAI peaks are not observed for the rest of the day. The PAI peaks do not return the following day, nor are they observed on June 25.

In order to better delineate the spatial extent of the region of steepened anisotropy, we directly compare similar passes (outbound and inbound) of Probes A and B. Figure 3 shows PAI vs. L* for three passes on June 26 (left) and June 27 (right) for electrons in the REPT 3.4 MeV energy channel. PAI from Probe A is shown in red and Probe B is shown in blue. On June 26, the top left panel shows Probe B in an outbound pass in the morning, ∼ 600−900 UT. The PAI are smoothly varying as the probe passes through the outer belt and are most peaked between 4.5 and 5 L*. By the time Probe A passes through the belt several hours later, a clear peak in PAI is seen, indicating a higher level of anisotropy in the 3.4 MeV energy channel at L*=5.1. As the probe passes through the outer belt, the anisotropy increases sharply at L*=5 (PAI∼2.6) reaching a maximum at L*=5.1 (PAI ∼3.2) and monotonically decreasing thereafter. On the subsequent inbound pass, shown in the middle left panel, both probes observe the PAI peak in the same location even though they are separated by 6 hours. On the next outbound pass (bottom left panel), Probe B observes the peak, while Probe A is not shown.

Similar features can be observed on the following day, with Probe B observing the PAI peak in the outbound pass while Probe A, visiting the same region earlier in time by several hours, does not (top right panel). Again, both probes observe the PAI peak in the same spatial location during their respective inbound passes (middle right panel), and by the next outbound pass (bottom right panel), the sudden storm commencement has occurred and the PAI peaks have vanished, as observed by both spacecraft.

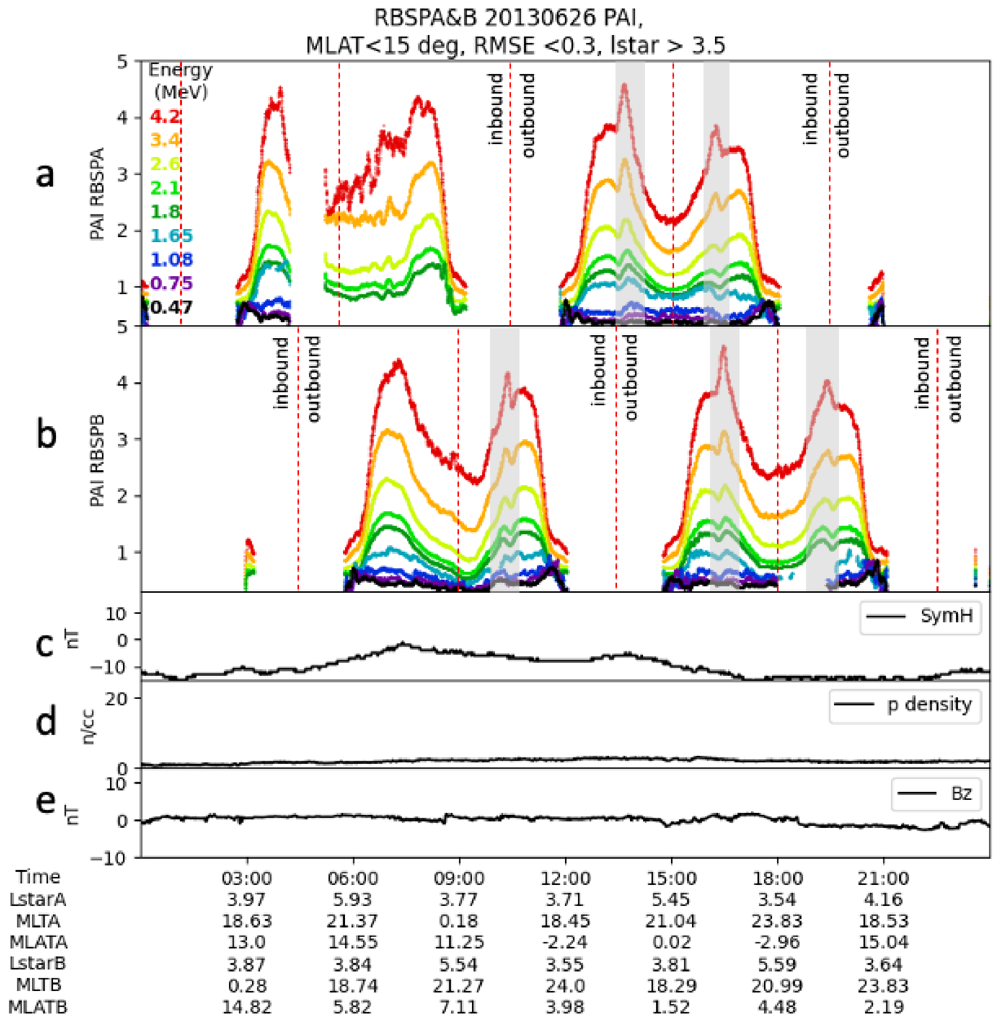

Figure 1. PAI summary plots for June 26, 2013. Panel a) shows PAI for Probe A for MagEIS and REPT energy channels (color indicates energy), panel b) is the same for Probe B. Panels c-e show SymH, p density and Bz from omniweb data. Time, L*, MLT, and MLAT are shown on the x-axis.

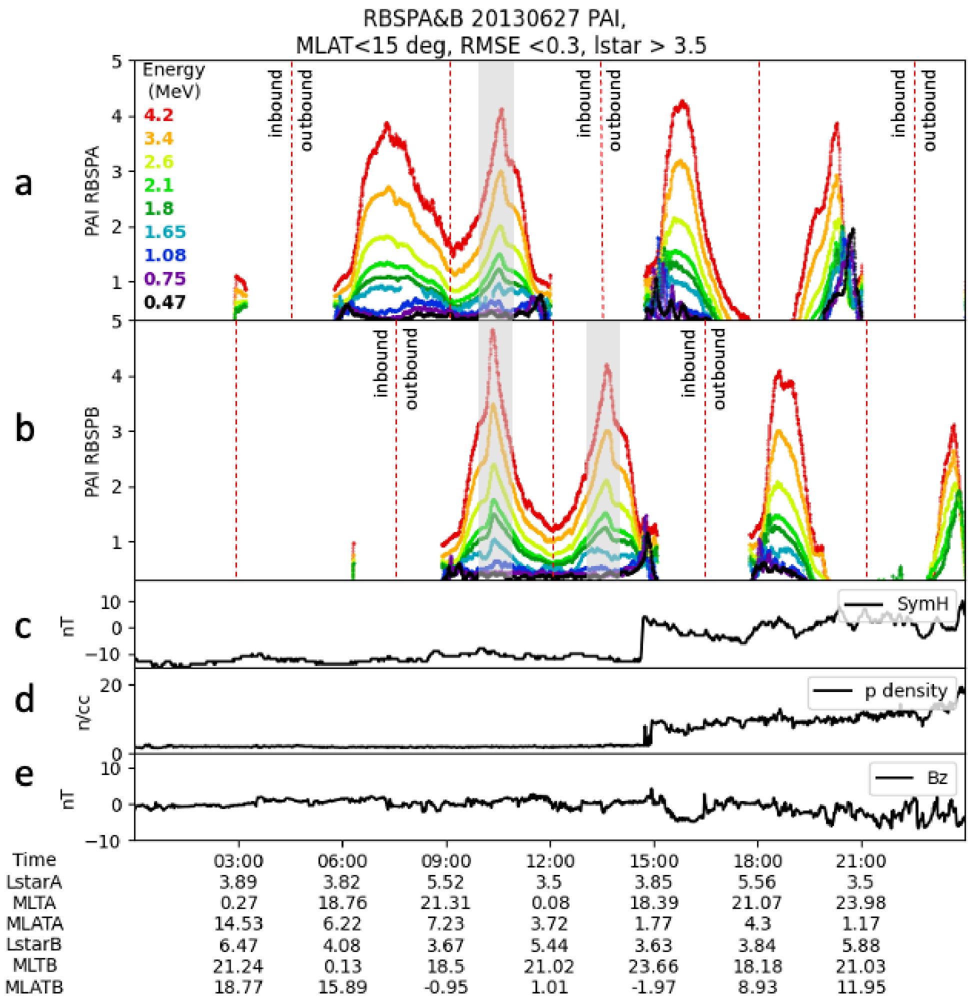

Figure 2. PAI summary plots for June 27, 2013. Panel a) shows PAI for Probe A for MagEIS and REPT energy channels (color indicating energy), panel b) is the same for Probe B. Panels c-e show SymH, p density and Bz from omniweb data. Time, L*, MLT, and MLAT are shown on the x-axis.

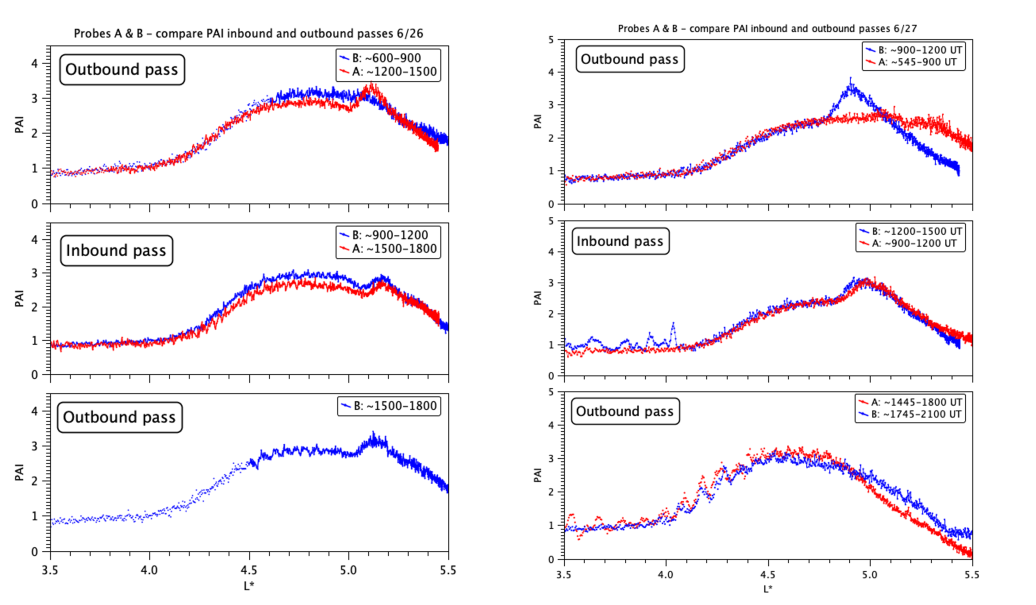

Figure 3. Comparing PAI vs. L* for Probe A and B passes for June 26 (left panels) and June 27 (right panels) in the 3.4 MeV electron channel. Probe B is in blue and Probe A is in red. For each, the top panel shows an outbound pass before the peaked feature and one after it occurs, the middle panel shows an inbound pass where both probes (separated in time) observe the peaked feature at the same spatial location, and then the following outbound pass. Indices in the upper right of the plot show time periods for each full pass.

These observations show that the PAI profiles have well defined features that persist for an extended period of time for both June 26 and 27. The steepened anisotropy in electron PADs that exist on both June 26 and June 27 are persistent in time over many orbital drifts of energetic electrons. For example, on June 27, the inbound passes of Probes A and B are about three hours apart. Electrons at L=5.5 and $\alpha_{eq} = 90°$ will drift approximately 45 times for 3.4 MeV electrons (4 minute drift period) and 25 time for 1.8 MeV electrons (7 minute drift period).

4 Discussion

From the foregoing, we conclude that either a) the electron anistropy itself is persistent and self sustaining, or b) there is a mechanism which creates the electron anisotropy that persists for an extended period of time. Peaked PADs may result from acceleration or loss, so it is useful to consider phase space density (PSD) calculations (Boyd et al., 2018, 2021) to determine the cause of the anisotropy. Figure 4 shows radial profiles of PSD for combined Probes A and B and several mu and k values for select orbits on June 26 and June 27. Mu values are 631 and 3981 MeV/G and k values are 0.11 and 0.02 $R_E G^{1/2}$. The energy associated with these values is indicated on a second axis under L*. They roughly cover the relativistic energy ranges on the lower boundary of the observed PAI peak as well as relativistic energies where the peak is strong. In addition, a k value of 0.11 $R_E G^{1/2}$ mirrors farther from the equator than a k value of 0.02 $R_E G^{1/2}$, showing the differences between the potentially precipitating and the near equatorial (not precipitating) populations. There are localized dropouts observed in panel c showing off-equatorial mirroring and ultra relativistic energies that are not observed closer to the equator or at energies <1.04 at L*=5. Though these dropouts are not especially strong

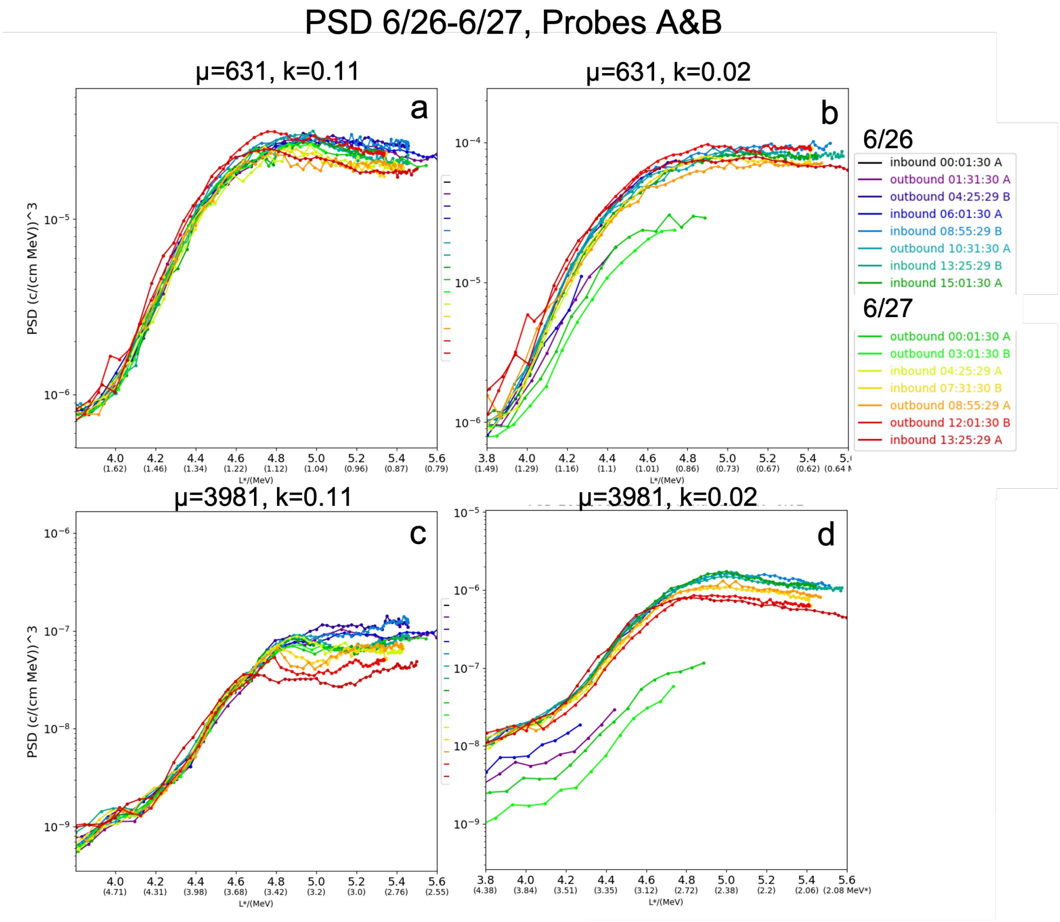

Figure 4. Phase space density profiles for mu values of 631 and 3981 MeV/G, and k values of 0.11 and 0.02 $R_E G^{1/2}$. In each panel, the colors indicate the passage of time over two days (selected orbits). k=0.11 $R_E G^{1/2}$ indicated off equatorial electrons while k=0.02 is close to equatorial. Mu=631 is ∼relativistic electron energy and mu=3981 is ultrarelativistic for L*=5. The energy for each mu value can be observed as a second axis under L*.

(< 1 order of magnitude), they are similar in size to changes in PSD previously associated with EMIC waves (Aseev et al., 2017). Importantly, Figure 4 shows no evidence of growing PSD peaks which would indicate energization (Green & Kivelson, 2004; Reeves et al., 1998). Figures showing time series of electron fluxes are included in the supplementary information which support the theory that the peaked PADs are due to loss during the indicated time periods.

The Van Allen Probes Emfisis data did not show significant wave activity during the period of interest (see supplementary information for spectral FFTs). However, this does not mean there were no EMIC waves along the drift orbit of the particles, since Van Allen Probes may not have been in a location to observe local wave activity and electron isotropies are observed due to electron drift. Both the probes were on the night side in the outer belts for the time period of interest. EMIC waves have a high occurrence during and after a storm main phase, with the strongest power in the noon to dusk region but occur across MLT (Halford et al., 2015; Saikin et al., 2015; Wang et al., 2015; Anderson & Hamilton, 1993).

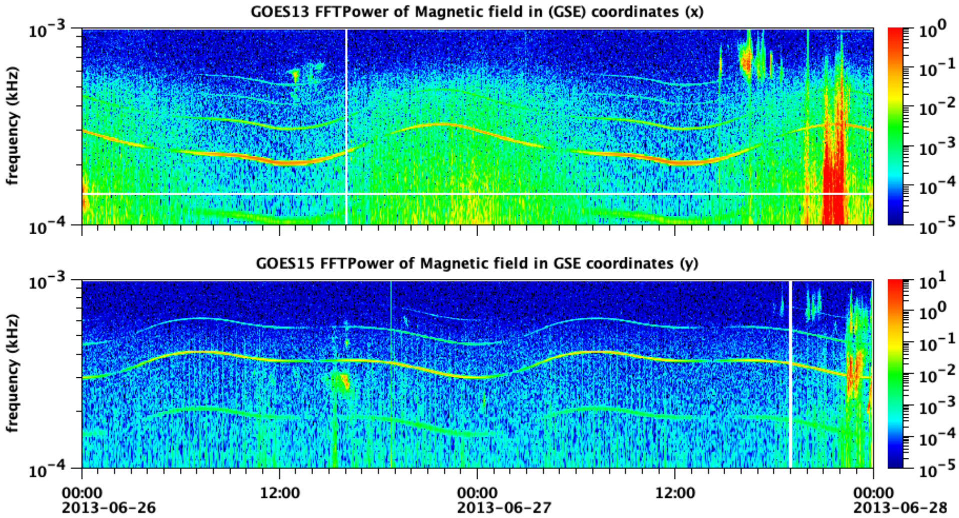

Figure 5. Spectral FFT for GOES13 (top) and GOES15 (bottom) for June 26 and 27. GOES13 observed EMIC waves 1200-1500 UT and GOES15 observes them 1500-1630 on June 26. Neither observes EMIC waves on June 27 until the storm commencement.

Alternatively, over the period of interest, GOES 13 and 15 both had full MLT coverage at L=6.6 and 6.8, respectively. Both Goes -13 and -15 are near geosynchronous orbit, a larger L value than those shown in the particle data, but both show evidence of EMIC waves on June 26. Figure 5 shows a spectral FFT for the EMIC frequency band for GOES13 (top) and GOES15 (bottom). GOES13 observes EMIC waves 1200-1500 UT and MLT of 7-9.5. GOES15 observes the waves 1500-1630 UT and at MLT of 5.6-7.3. GOES13 and 15 observe EMIC waves during the time period of the anisotropy on June 26, but due to the long orbital period of the satellites (1 day), the persistence of the EMIC waves is not clear. Neither satellite observes EMIC waves on June 27 until the storm commencement. However, the satellites are located near midnight in MLT when the anisotropy occurs on June 27, so again observations may be limited by spacecraft coverage.

In-situ observations of near-simultaneous wave activity and concomitant PAD changes are difficult, due, for example, to distinct spatial and temporal location and occurrence of particle and wave activity ,respectively. To some extent, this can be overcome by the use of ground based wave activity measurements. However, EMIC waves in space are both modulated and ducted when they are observed on the ground, thereby complicating associating wave activity with particle PAD observations (Upadhyay et al., 2022; Pakhotin et al., 2022).

The CARISMA (in North America) and SGO (in Finland) network of ground magnetometer stations can be useful in further exploration of the EMIC wave activity. Several stations in both networks observe pulsations in PC bands 1 and 2, indicating EMIC waves (Kennel & Petschek, 1966; Engebretson et al., 2002). Figure 6 shows spectral FFT for six stations from CARISMA and 4 stations from SGO on June 26 and June 27 that show clear indications of EMIC waves. From top to bottom, the stations in the left panel are YKC (Yellowknife), FCC (Fort Churchhill), FSMI (Fort Smith), LARG (La Ronge), TPAS (The Pas), and MSTK (Ministik Lake). SGO stations, on the right are KIL (Kilpisjarvi), IVA (Ivalo), SOD (Sodankyla), and OUL (Oulu), Their L-shells, in the same order, are 7.85, 7.16, 6.64, 5.04, 4.83, 4.13 (left) (K. Murphy, 2022; K. R. Murphy et al., 2022) and 6.2, 5.9, 5.4, 5.2 (right). Collectively, they observe these waves for an extended period of time on June 26, namely 1000-2200 UT, which is the same time period of observed steepened anisotropy in the Van Allen Probes particle data. On June 27, CARISMA does not observe EMIC wave activity until 1500 UT, which is the same time as the SSC. Similar to the GOES satellites, these ground stations were close to midnight during the PAI peaks on June 27. SGO stations briefly observe pulsations at 400-900 UT on June 27, but also were not on the morning side after this time period. A detailed survey of other ground stations showed that data was not available from other stations at the necessary frequencies to draw any conclusions regarding waves on June 27 during the time period 1000-1400 UT.

Figure 7 shows two dial plots and a L vs. time plot for June 26 and June 27. The plots show the orbits and mapped ground magnetometer stations to L and MLT. In all three panels, Van Allen Probes orbits are in green, with the location of the PAI peaks indicated with black markers. GOES13 and 15 orbits are shown in blue, with observed EMIC waves in red markers. An approximate extent of the EMIC waves observed by the Carisma stations (June 26) and SGO stations (June 26 and June 27) are shown in an outlined gray box. Note that EMIC waves can duct in the ionosphere, creating a wider range of spatial measurements on the ground compared to their in-situ location (Mann et al., 2014). Therefore, the ground measurements only give a rough estimation of the EMIC wave locations but can be useful when there are insufficient satellite observations to determine the duration of EMIC wave activity. While the EMIC wave observations are in a different MLT sector than the PAI peaks, they are well associated in time and L-shell on June 26. On June 27, they are well associated in L-shell, but there are not enough measurements to determine their time and spatial extent in the magnetosphere.

EMIC waves cause scattering of off equatorial electrons at relativistic and ultra relativistic energies (Bingley et al., 2019; Summers et al., 2007; Ni, Cao, et al., 2015), which can account for the PAI peak observed at the >1 MeV energies as seen by the Van Allen Probes. EMIC waves also tend to be spatially confined but can persist for many hours (Mann et al., 2014; Paulson et al., 2017; Blum & Breneman, 2020). They are a likely cause of the unique PAI observed on June 26 and 27. The anisotropy peaks are similar on these two days even though strong indication of EMIC waves is only observed on the first day. It is likely that the long-lasting anisotropy is caused by the persistent EMIC waves. While the EMIC waves themselves are spatially confined, they have a long lasting a global effect on the radiation belts, as the particle affect is observed in a separate location from the waves. The particle anisotropies were observed in two satellites on the night-side, while EMIC waves were separately observed by two satellites and many ground stations near the morning/noon sector. Combining multipoint measurements was integral to understanding this isolated event. In addition, in the absence of other processes, signatures of wave-particle processes can be long lasting, highlighting the importance of studying the dynamics and strength of these interactions during quiet times (as opposed to storm times) when they can be more easily quantified and don't need to separated out from other processes. More measurements and case studies could give greater weight to this already strong association.

5 Summary

In this study, we showed PAI changes on two days, June 26 and 27, 2013, that were spatially confined and persisted for a significant amount of time in terms of drift periods of relativistic and ultrarelativistic electrons. These PAI changes existed for a wide range of electron energies as observed by both MagEIS and REPT on the Van Allen Probes and across both probes, down to $\sim 500keV$. This was during an otherwise quiet time in the magnetosphere (until 1500 UT on June 27, when there was a SSC). Our analysis of phase space density suggests that these steepened anisotropies of electrons are a result of electron loss at low pitch angles rather than an enhancement near 90°.

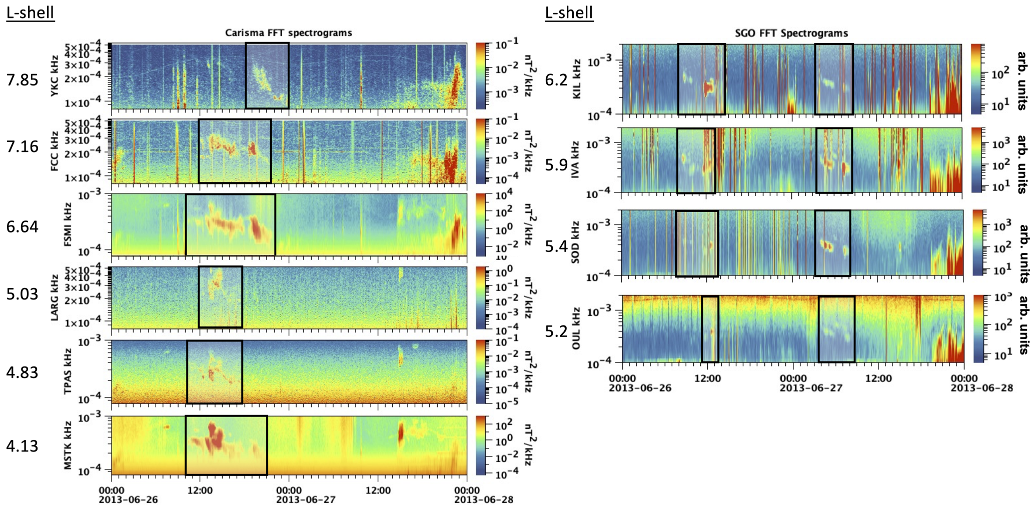

Figure 6. Spectral FFT for CARISMA and SGO stations on June 26 and 27. Power is indicated by color. Black boxes highlight the region with PC1-2 band pulsations associated with EMIC waves. The L-shell of each station is shown on the left.

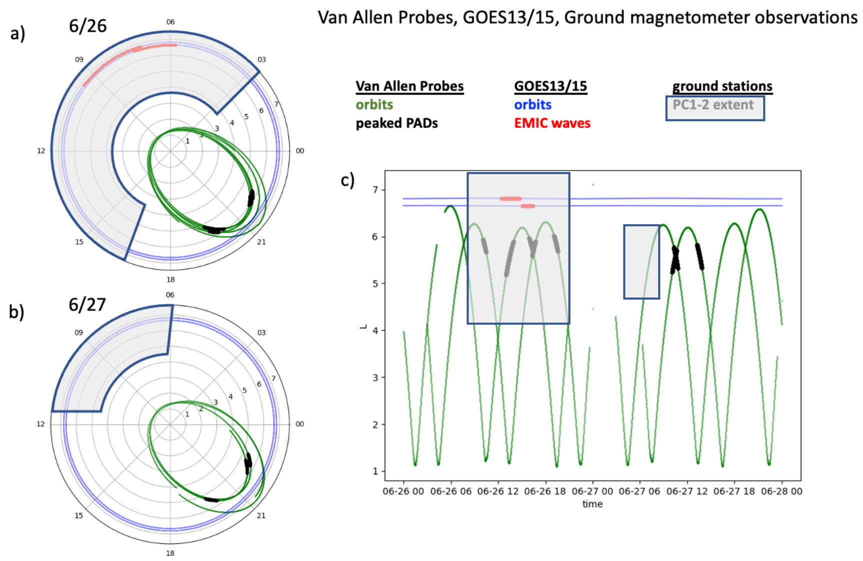

Figure 7. Dial plot and Lshell vs. time. Panels a and b show Lshell vs. MLT for June 26 and 27 (respectively). Panel c shows Lshell vs time for both days and multi-measurement locations.

Van Allen Probes did not observe significant wave activity during these two days, however, GOES13 and 15 observed brief periods of EMIC wave activity. Furthermore, ground magnetometer stations in North America and Finland observed long term fluctuations in the PC bands associated with EMIC waves. EMIC waves are known to scatter > relativistic electrons into the loss cone, and the observed EMIC activity persists during the time period on June 26 overlapping when the steepened electron pitch angle anisotropy peaks are observed. There is some evidence of wave activity on June 27 at an earlier time period than the strong anisotropies, but the lack of PC pulsations during the anistropy during this time period is possibly due to limitations of accessible data during the region and time period of interest. Our results suggest that a period of spatially localized EMIC waves in the dawn-noon sector caused a long lasting steepening of the pitch angle index, isolated in L-shell but global in magnetic local time. It is therefore important to study the dynamics of EMIC wave interactions with energetic electrons during quiet periods as well as storm times, and to include events that don't have clear wave satellite observations. PAI is a useful tool for clearly finding regions of changing PADs and associating them with radiation belt mechanisms.

6 Open Research

The authors thank I.R. Mann, D.K. Milling and the rest of the CARISMA team for data. CARISMA is operated by the University of Alberta, funded by the Canadian Space Agency. CARISMA data can be found at https://carisma.ca/. Van Allen Probes and OMNIWeb data can be found through NASA's Space Physics Data Facility (SPDF) at https://spdf.gsfc.nasa.gov/. The authors thank T. Raita for data access, and more information on SGO data and overview plots can be found at https://www.sgo.fi/index.php. Processing software for PAD fits can be found online by A. Greeley (2023).

Acknowledgments
The authors would like to thank the International Space Science Institute's (ISSI) International Teams program for support. A.D. Greeley, S.G. Kanekal, L. Blum, A. Halford, and K. Murphy are supported by and work with the Space Precipitation Impacts project at Goddard Space Flight Center through the Heliophysics Internal Science Funding Model.

References

Abel, B., & Thorne, R. M. (1998). Electron scattering loss in earth's inner magnetosphere: 1. dominant physical processes. *Journal of Geophysical Research: Space Physics*, *103*(A2), 2385-2396. Retrieved from `https://agupubs.onlinelibrary.wiley.com/doi/abs/10.1029/97JA02919` doi: https://doi.org/10.1029/97JA02919

Anderson, B. J., Erlandson, R. E., & Zanetti, L. J. (1992). A statistical study of pc 1–2 magnetic pulsations in the equatorial magnetosphere: 1. equatorial occurrence distributions. *Journal of Geophysical Research: Space Physics*, *97*(A3), 3075-3088. Retrieved from `https://agupubs.onlinelibrary.wiley.com/doi/abs/10.1029/91JA02706` doi: https://doi.org/10.1029/91JA02706

Anderson, B. J., & Hamilton, D. C. (1993). Electromagnetic ion cyclotron waves stimulated by modest magnetospheric compressions. *Journal of Geophysical Research: Space Physics*, *98*(A7), 11369-11382. Retrieved from `https://agupubs.onlinelibrary.wiley.com/doi/abs/10.1029/93JA00605` doi: https://doi.org/10.1029/93JA00605

Aseev, N. A., Shprits, Y. Y., Drozdov, A. Y., Kellerman, A. C., Usanova, M. E., Wang, D., & Zhelavskaya, I. S. (2017). Signatures of ultrarelativistic electron loss in the heart of the outer radiation belt measured by van allen probes.

Journal of Geophysical Research: Space Physics, *122*(10), 10,102-10,111. Retrieved from https://agupubs.onlinelibrary.wiley.com/doi/abs/10.1002/2017JA024485 doi: https://doi.org/10.1002/2017JA024485

Baker, D. N. (2021, October). Wave–particle interaction effects in the Van Allen belts. *Earth, Planets and Space*, *73*(1), 189. Retrieved from https://doi.org/10.1186/s40623-021-01508-y doi: 10.1186/s40623-021-01508-y

Baker, D. N., Kanekal, S. G., Hoxie, V., Li, X., Jaynes, A. N., Zhao, H., ... Filwett, R. (2021, July). The Relativistic Electron-Proton Telescope (REPT) Investigation: Design, Operational Properties, and Science Highlights. *Space Science Reviews*, *217*(5), 68. Retrieved from https://doi.org/10.1007/s11214-021-00838-3 doi: 10.1007/s11214-021-00838-3

Baker, D. N., Li, X., Blake, J. B., & Kanekal, S. (1998). Strong electron acceleration in the Earth's magnetosphere. *Advances in Space Research*, *21*(4), 609–613. Retrieved from https://www.sciencedirect.com/science/article/pii/S0273117797009708 doi: https://doi.org/10.1016/S0273-1177(97)00970-8

Baker, D. N., et al. (2012). The relativistic electron-proton telescope (rept) instrument on board the radiation belt storm probes (rbsp) spacecraft: Characterization of earth's radiation belt high-energy particle populations. *Space Sci. Rev.*, *179*, 1-4. doi: 10.1007/s11214-012-9950-9

Bingley, L., Angelopoulos, V., Sibeck, D., Zhang, X., & Halford, A. (2019). The evolution of a pitch-angle "bite-out" scattering signature caused by emic wave activity: A case study. *Journal of Geophysical Research: Space Physics*, *124*(7), 5042-5055. Retrieved from https://agupubs.onlinelibrary.wiley.com/doi/abs/10.1029/2018JA026292 doi: https://doi.org/10.1029/2018JA026292

Blake, J. B., Carranza, P. A., Claudepierre, S. G., Clemmons, J. H., Crain, W. R., Dotan, Y., ... Zakrzewski, M. P. (2013, November). The Magnetic Electron Ion Spectrometer (MagEIS) Instruments Aboard the Radiation Belt Storm Probes (RBSP) Spacecraft. *Space Science Reviews*, *179*(1), 383–421. Retrieved from https://doi.org/10.1007/s11214-013-9991-8 doi: 10.1007/s11214-013-9991-8

Blum, L. W., & Breneman, A. W. (2020). Chapter 3 - observations of radiation belt losses due to cyclotron wave-particle interactions. In A. N. Jaynes & M. E. Usanova (Eds.), *The dynamic loss of earth's radiation belts* (p. 49-98). Elsevier. Retrieved from https://www.sciencedirect.com/science/article/pii/B9780128133712000032 doi: https://doi.org/10.1016/B978-0-12-813371-2.00003-2

Blum, L. W., Halford, A., Millan, R., Bonnell, J. W., Goldstein, J., Usanova, M., ... Li, X. (2015). Observations of coincident emic wave activity and duskside energetic electron precipitation on 18–19 january 2013. *Geophysical Research Letters*, *42*(14), 5727-5735. Retrieved from https://agupubs.onlinelibrary.wiley.com/doi/abs/10.1002/2015GL065245 doi: https://doi.org/10.1002/2015GL065245

Boyd, A. J., Spence, H. E., Reeves, G. D., Funsten, H. O., Skoug, R. M., Larsen, B. A., ... Jaynes, A. N. (2021). Rbsp-ect combined pitch angle resolved electron flux data product. *Journal of Geophysical Research: Space Physics*, *126*(3), e2020JA028637. Retrieved from https://agupubs.onlinelibrary.wiley.com/doi/abs/10.1029/2020JA028637 (e2020JA028637 2020JA028637) doi: https://doi.org/10.1029/2020JA028637

Boyd, A. J., Turner, D. L., Reeves, G. D., Spence, H. E., Baker, D. N., & Blake, J. B. (2018). What causes radiation belt enhancements: A survey of the van allen probes era. *Geophysical Research Letters*, *45*(11), 5253-5259. Retrieved from https://agupubs.onlinelibrary.wiley.com/doi/abs/10.1029/2018GL077699 doi: https://doi.org/10.1029/2018GL077699

Claudepierre, S. G., Blake, J. B., Boyd, A. J., Clemmons, J. H., Fennell, J. F., Gabrielse, C., … Turner, D. L. (2021, October). The Magnetic Electron Ion Spectrometer: A Review of On-Orbit Sensor Performance, Data, Operations, and Science. *Space Science Reviews*, *217*(8), 80. Retrieved from `https://doi.org/10.1007/s11214-021-00855-2` doi: 10.1007/s11214-021-00855-2

Claudepierre, S. G., Ma, Q., Bortnik, J., O'Brien, T. P., Fennell, J. F., & Blake, J. B. (2020). Empirically estimated electron lifetimes in the earth's radiation belts: Comparison with theory. *Geophysical Research Letters*, *47*(3), e2019GL086056. Retrieved from `https://agupubs.onlinelibrary.wiley.com/doi/abs/10.1029/2019GL086056` (e2019GL086056 10.1029/2019GL086056) doi: https://doi.org/10.1029/2019GL086056

Engebretson, M. J., Peterson, W. K., Posch, J. L., Klatt, M. R., Anderson, B. J., Russell, C. T., … Fukunishi, H. (2002). Observations of two types of pc 1–2 pulsations in the outer dayside magnetosphere. *Journal of Geophysical Research: Space Physics*, *107*(A12), SMP 20-1-SMP 20-20. Retrieved from `https://agupubs.onlinelibrary.wiley.com/doi/abs/10.1029/2001JA000198` doi: https://doi.org/10.1029/2001JA000198

Fennell, J. F., Roeder, J. L., Kurth, W. S., Henderson, M. G., Larsen, B. A., Hospodarsky, G., … Reeves, G. D. (2014). Van allen probes observations of direct wave-particle interactions. *Geophysical Research Letters*, *41*(6), 1869-1875. Retrieved from `https://agupubs.onlinelibrary.wiley.com/doi/abs/10.1002/2013GL059165` doi: https://doi.org/10.1002/2013GL059165

Gannon, J. L., Li, X., & Heynderickx, D. (2007). Pitch angle distribution analysis of radiation belt electrons based on combined release and radiation effects satellite medium electrons a data. *Journal of Geophysical Research: Space Physics*, *112*(A5). Retrieved from `https://agupubs.onlinelibrary.wiley.com/doi/abs/10.1029/2005JA011565` doi: https://doi.org/10.1029/2005JA011565

Greeley, A. (2023, March). *ashleygreeley/sin_pads: sin_pads.* Zenodo. Retrieved from `https://doi.org/10.5281/zenodo.7775926` doi: 10.5281/zenodo.7775926

Greeley, A. D., Kanekal, S. G., Baker, D. N., Klecker, B., & Schiller, Q. (2019). Quantifying the contribution of microbursts to global electron loss in the radiation belts. *Journal of Geophysical Research: Space Physics*, *124*(2), 1111-1124. Retrieved from `https://agupubs.onlinelibrary.wiley.com/doi/abs/10.1029/2018JA026368` doi: https://doi.org/10.1029/2018JA026368

Greeley, A. D., Kanekal, S. G., Sibeck, D. G., Schiller, Q., & Baker, D. N. (2021). Evolution of pitch angle distributions of relativistic electrons during geomagnetic storms: Van allen probes observations. *Journal of Geophysical Research: Space Physics*, *126*(2), e2020JA028335. Retrieved from `https://agupubs.onlinelibrary.wiley.com/doi/abs/10.1029/2020JA028335` (e2020JA028335 2020JA028335) doi: https://doi.org/10.1029/2020JA028335

Green, J. C., & Kivelson, M. G. (2004). Relativistic electrons in the outer radiation belt: Differentiating between acceleration mechanisms. *Journal of Geophysical Research: Space Physics*, *109*(A3). Retrieved from `https://agupubs.onlinelibrary.wiley.com/doi/abs/10.1029/2003JA010153` doi: https://doi.org/10.1029/2003JA010153

Halford, A. J., Fraser, B. J., & Morley, S. K. (2015). Emic waves and plasmaspheric and plume density: Crres results. *Journal of Geophysical Research: Space Physics*, *120*(3), 1974-1992. Retrieved from `https://agupubs.onlinelibrary.wiley.com/doi/abs/10.1002/2014JA020338` doi: https://doi.org/10.1002/2014JA020338

Horne, R. B., & Thorne, R. M. (2003). Relativistic electron acceleration and precipitation during resonant interactions with whistler-mode chorus. *Geophysical Research Letters*, *30*(10). Retrieved from `https://agupubs.onlinelibrary.wiley.com/doi/abs/10.1029/2003GL016973` doi: https://doi.org/10.1029/2003GL016973

Jacobs, J. A., Kato, Y., Matsushita, S., & Troitskaya, V. A. (1964). Classification of geomagnetic micropulsations. *Journal of Geophysical Research (1896-1977)*, *69*(1), 180-181. Retrieved from https://agupubs.onlinelibrary.wiley.com/doi/abs/10.1029/JZ069i001p00180 doi: https://doi.org/10.1029/JZ069i001p00180

Jaynes, A. N., Baker, D. N., Singer, H. J., Rodriguez, J. V., Loto'aniu, T. M., Ali, A. F., … Reeves, G. D. (2015). Source and seed populations for relativistic electrons: Their roles in radiation belt changes. *Journal of Geophysical Research: Space Physics*, *120*(9), 7240-7254. Retrieved from https://agupubs.onlinelibrary.wiley.com/doi/abs/10.1002/2015JA021234 doi: https://doi.org/10.1002/2015JA021234

Kanekal, S., & Miyoshi, Y. (2021, May). Dynamics of the terrestrial radiation belts: a review of recent results during the VarSITI (Variability of the Sun and Its Terrestrial Impact) era, 2014–2018. *Progress in Earth and Planetary Science*, *8*(1), 35. Retrieved from https://doi.org/10.1186/s40645-021-00413-y doi: 10.1186/s40645-021-00413-y

Kanekal, S. G., Friedel, R. H. W., Reeves, G. D., Baker, D. N., & Blake, J. B. (2005). Relativistic electron events in 2002: Studies of pitch angle isotropization. *Journal of Geophysical Research: Space Physics*, *110*(A12). Retrieved from https://agupubs.onlinelibrary.wiley.com/doi/abs/10.1029/2004JA010974 doi: https://doi.org/10.1029/2004JA010974

Kasahara, S., Miyoshi, Y., Yokota, S., Mitani, T., Kasahara, Y., Matsuda, S., … Shinohara, I. (2018, February). Pulsating aurora from electron scattering by chorus waves. *Nature*, *554*(7692), 337–340. Retrieved from https://doi.org/10.1038/nature25505 doi: 10.1038/nature25505

Kennel, C. F., & Petschek, H. E. (1966). Limit on stably trapped particle fluxes. *Journal of Geophysical Research (1896-1977)*, *71*(1), 1-28. Retrieved from https://agupubs.onlinelibrary.wiley.com/doi/abs/10.1029/JZ071i001p00001 doi: https://doi.org/10.1029/JZ071i001p00001

Kubota, Y., & Omura, Y. (2017). Rapid precipitation of radiation belt electrons induced by emic rising tone emissions localized in longitude inside and outside the plasmapause. *Journal of Geophysical Research: Space Physics*, *122*(1), 293-309. Retrieved from https://agupubs.onlinelibrary.wiley.com/doi/abs/10.1002/2016JA023267 doi: https://doi.org/10.1002/2016JA023267

Mann, I. R., Milling, D. K., Rae, I. J., Ozeke, L. G., Kale, A., Kale, Z. C., … Singer, H. J. (2008, December). The Upgraded CARISMA Magnetometer Array in the THEMIS Era. *Space Science Reviews*, *141*(1), 413–451. Retrieved from https://doi.org/10.1007/s11214-008-9457-6 doi: 10.1007/s11214-008-9457-6

Mann, I. R., Usanova, M. E., Murphy, K., Robertson, M. T., Milling, D. K., Kale, A., … Raita, T. (2014). Spatial localization and ducting of emic waves: Van allen probes and ground-based observations. *Geophysical Research Letters*, *41*(3), 785-792. Retrieved from https://agupubs.onlinelibrary.wiley.com/doi/abs/10.1002/2013GL058581 doi: https://doi.org/10.1002/2013GL058581

Mauk, B. H., Fox, N. J., Kanekal, S. G., Kessel, R. L., Sibeck, D. G., & Ukhorskiy, A. (2013, Nov 01). Science objectives and rationale for the radiation belt storm probes mission. *Space Science Reviews*, *179*(1), 3–27. Retrieved from https://doi.org/10.1007/s11214-012-9908-y doi: 10.1007/s11214-012-9908-y

Medeiros, C., Souza, V. M., Vieira, L. E. A., Sibeck, D. G., Halford, A. J., Kang, S.-B., … Kletzing, C. A. (2019, February). On the contribution of EMIC waves to the reconfiguration of the relativistic electron butterfly pitch angle distribution shape on 2014 september 12—a case study. *The Astrophysical Journal*, *872*(1), 36. Retrieved from https://doi.org/10.3847/1538-4357/aaf970 doi: 10.3847/1538-4357/aaf970

Murphy, K. (2022, June). *kylermurphy/gmag: Gmag frontiers initial release.* Zenodo. Retrieved from https://doi.org/10.5281/zenodo.6686035 doi: 10.5281/zenodo.6686035

Murphy, K. R., Rae, I. J., Halford, A. J., Engebretson, M., Russell, C. T., Matzka, J., … Tanskanen, E. (2022). Gmag: An open-source python package for ground-based magnetometers. *Frontiers in Astronomy and Space Sciences*, *9*. Retrieved from https://www.frontiersin.org/articles/10.3389/fspas.2022.1005061 doi: 10.3389/fspas.2022.1005061

Nakamura, S., Miyoshi, Y., Shiokawa, K., Omura, Y., Mitani, T., Takashima, T., … Angelopoulos, V. (2022). Simultaneous observations of emic-induced drifting electron holes (edehs) in the earth's radiation belt by the arase satellite, van allen probes, and themis. *Geophysical Research Letters*, *49*(5), e2021GL095194. Retrieved from https://agupubs.onlinelibrary.wiley.com/doi/abs/10.1029/2021GL095194 (e2021GL095194 2021GL095194) doi: https://doi.org/10.1029/2021GL095194

Ni, B., Bortnik, J., Thorne, R. M., Ma, Q., & Chen, L. (2013). Resonant scattering and resultant pitch angle evolution of relativistic electrons by plasmaspheric hiss. *Journal of Geophysical Research: Space Physics*, *118*(12), 7740-7751. Retrieved from https://agupubs.onlinelibrary.wiley.com/doi/abs/10.1002/2013JA019260 doi: https://doi.org/10.1002/2013JA019260

Ni, B., Cao, X., Zou, Z., Zhou, C., Gu, X., Bortnik, J., … Xie, L. (2015). Resonant scattering of outer zone relativistic electrons by multiband emic waves and resultant electron loss time scales. *Journal of Geophysical Research: Space Physics*, *120*(9), 7357-7373. Retrieved from https://agupubs.onlinelibrary.wiley.com/doi/abs/10.1002/2015JA021466 doi: https://doi.org/10.1002/2015JA021466

Ni, B., Zou, Z., Gu, X., Zhou, C., Thorne, R. M., Bortnik, J., … Li, X. (2015). Variability of the pitch angle distribution of radiation belt ultrarelativistic electrons during and following intense geomagnetic storms: Van allen probes observations. *Journal of Geophysical Research: Space Physics*, *120*(6), 4863-4876. Retrieved from https://agupubs.onlinelibrary.wiley.com/doi/abs/10.1002/2015JA021065 doi: https://doi.org/10.1002/2015JA021065

Pakhotin, I. P., Mann, I. R., Sydorenko, D., & Rankin, R. (2022). Novel emic wave propagation pathway through buchsbaum resonance and interhemispheric wave interference: Swarm observations and modeling. *Geophysical Research Letters*, *49*(10), e2022GL098249. Retrieved from https://agupubs.onlinelibrary.wiley.com/doi/abs/10.1029/2022GL098249 (e2022GL098249 2022GL098249) doi: https://doi.org/10.1029/2022GL098249

Paulson, K. W., Smith, C. W., Lessard, M. R., Torbert, R. B., Kletzing, C. A., & Wygant, J. R. (2017). In situ statistical observations of pc1 pearl pulsations and unstructured emic waves by the van allen probes. *Journal of Geophysical Research: Space Physics*, *122*(1), 105-119. Retrieved from https://agupubs.onlinelibrary.wiley.com/doi/abs/10.1002/2016JA023160 doi: https://doi.org/10.1002/2016JA023160

Reeves, G. D., Baker, D. N., Belian, R. D., Blake, J. B., Cayton, T. E., Fennell, J. F., … Spence, H. E. (1998). The global response of relativistic radiation belt electrons to the january 1997 magnetic cloud. *Geophysical Research Letters*, *25*(17), 3265-3268. Retrieved from https://agupubs.onlinelibrary.wiley.com/doi/abs/10.1029/98GL02509 doi: https://doi.org/10.1029/98GL02509

Reeves, G. D., Spence, H. E., Henderson, M. G., Morley, S. K., Friedel, R. H. W., Funsten, H. O., … Niehof, J. T. (2013). Electron acceleration in the heart of the van allen radiation belts. *Science*, *341*(6149), 991-994. Retrieved from https://www.science.org/doi/abs/10.1126/science.1237743 doi: 10.1126/science.1237743

Saikin, A. A., Zhang, J.-C., Allen, R. C., Smith, C. W., Kistler, L. M., Spence, H. E., . . . Jordanova, V. K. (2015). The occurrence and wave properties of h+-, he+-, and o+-band emic waves observed by the van allen probes. *Journal of Geophysical Research: Space Physics*, *120*(9), 7477-7492. Retrieved from https://agupubs.onlinelibrary.wiley.com/doi/abs/10.1002/2015JA021358 doi: https://doi.org/10.1002/2015JA021358

Spence, H. E., Reeves, G. D., Baker, D. N., Blake, J. B., Bolton, M., Bourdarie, S., . . . Thorne, R. M. (2013, November). Science Goals and Overview of the Radiation Belt Storm Probes (RBSP) Energetic Particle, Composition, and Thermal Plasma (ECT) Suite on NASA's Van Allen Probes Mission. *Space Science Reviews*, *179*(1), 311–336. Retrieved from https://doi.org/10.1007/s11214-013-0007-5 doi: 10.1007/s11214-013-0007-5

Summers, D., Ni, B., & Meredith, N. P. (2007). Timescales for radiation belt electron acceleration and loss due to resonant wave-particle interactions: 2. evaluation for vlf chorus, elf hiss, and electromagnetic ion cyclotron waves. *Journal of Geophysical Research: Space Physics*, *112*(A4). Retrieved from https://agupubs.onlinelibrary.wiley.com/doi/abs/10.1029/2006JA011993 doi: https://doi.org/10.1029/2006JA011993

Thorne, R. M. (2010). Radiation belt dynamics: The importance of wave-particle interactions. *Geophysical Research Letters*, *37*(22). Retrieved from https://agupubs.onlinelibrary.wiley.com/doi/abs/10.1029/2010GL044990 doi: https://doi.org/10.1029/2010GL044990

Thorne, R. M., Bortnik, J., Li, W., & Ma, Q. (2021). Wave–particle interactions in the earth's magnetosphere. In *Magnetospheres in the solar system* (p. 93-108). American Geophysical Union (AGU). Retrieved from https://agupubs.onlinelibrary.wiley.com/doi/abs/10.1002/9781119815624.ch6 doi: https://doi.org/10.1002/9781119815624.ch6

Upadhyay, A., Kakad, B., Kakad, A., & Rawat, R. (2022). A statistical study of modulation of electromagnetic ion cyclotron waves observed on ground. *Journal of Geophysical Research: Space Physics*, *127*(8), e2022JA030340. Retrieved from https://agupubs.onlinelibrary.wiley.com/doi/abs/10.1029/2022JA030340 (e2022JA030340 2022JA030340) doi: https://doi.org/10.1029/2022JA030340

Usanova, M. E., & Blum, L. W. (2021). Analysis of conjugate satellite and ground emic wave observations. In *2021 usnc-ursi radio science meeting (uscn-ursi rsm)* (p. 058-058). doi: 10.23919/USNC-URSIRSM52661.2021.9552374

Usanova, M. E., Drozdov, A., Orlova, K., Mann, I. R., Shprits, Y., Robertson, M. T., . . . Wygant, J. (2014). Effect of emic waves on relativistic and ultrarelativistic electron populations: Ground-based and van allen probes observations. *Geophysical Research Letters*, *41*(5), 1375-1381. Retrieved from https://agupubs.onlinelibrary.wiley.com/doi/abs/10.1002/2013GL059024 doi: https://doi.org/10.1002/2013GL059024

Wang, D., Yuan, Z., Yu, X., Deng, X., Zhou, M., Huang, S., . . . Wygant, J. R. (2015). Statistical characteristics of emic waves: Van allen probe observations. *Journal of Geophysical Research: Space Physics*, *120*(6), 4400-4408. Retrieved from https://agupubs.onlinelibrary.wiley.com/doi/abs/10.1002/2015JA021089 doi: https://doi.org/10.1002/2015JA021089

West Jr., H. I., Buck, R. M., & Walton, J. R. (1973). Electron pitch angle distributions throughout the magnetosphere as observed on ogo 5. *Journal of Geophysical Research (1896-1977)*, *78*(7), 1064-1081. Retrieved from https://agupubs.onlinelibrary.wiley.com/doi/abs/10.1029/JA078i007p01064 doi: https://doi.org/10.1029/JA078i007p01064

Zhang, J., Halford, A. J., Saikin, A. A., Huang, C.-L., Spence, H. E., Larsen, B. A., . . . Baker, D. N. (2016). Emic waves and associated relativistic electron precipitation on 25–26 january 2013. *Journal of Geophysical Re-*

search: Space Physics, *121*(11), 11,086-11,100. Retrieved from https://agupubs.onlinelibrary.wiley.com/doi/abs/10.1002/2016JA022918 doi: https://doi.org/10.1002/2016JA022918

Zhao, H., Friedel, R. H. W., Chen, Y., Reeves, G. D., Baker, D. N., Li, X., ... Spence, H. E. (2018). An empirical model of radiation belt electron pitch angle distributions based on van allen probes measurements. *Journal of Geophysical Research: Space Physics*, *123*(5), 3493-3511. Retrieved from https://agupubs.onlinelibrary.wiley.com/doi/abs/10.1029/2018JA025277 doi: https://doi.org/10.1029/2018JA025277

Zhao, H., Johnston, W. R., Baker, D. N., Li, X., Ni, B., Jaynes, A. N., ... Boyd, A. J. (2019). Characterization and evolution of radiation belt electron energy spectra based on the van allen probes measurements. *Journal of Geophysical Research: Space Physics*, *124*(6), 4217-4232. Retrieved from https://agupubs.onlinelibrary.wiley.com/doi/abs/10.1029/2019JA026697 doi: https://doi.org/10.1029/2019JA026697

Figure 1.

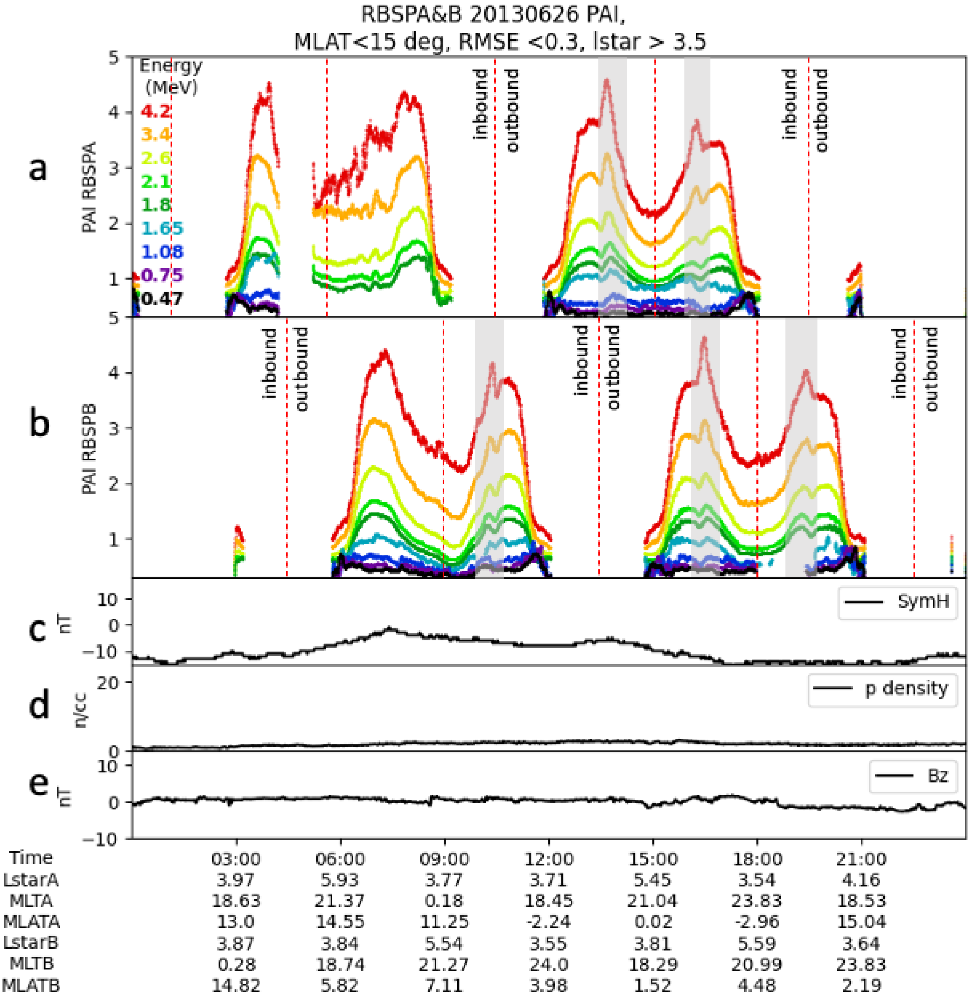
RBSPA&B 20130626 PAI,
MLAT<15 deg, RMSE <0.3, lstar > 3.5
Energy (MeV)
4.2
3.4
2.6
2.1
1.8
1.65
1.08
0.75
0.47
inbound
outbound
a
PAI RBSPA
b
PAI RBSPB
c
nT
SymH
d
n/cc
p density
e
Bz
Time 03:00 06:00 09:00 12:00 15:00 18:00 21:00
LstarA 3.97 5.93 3.77 3.71 5.45 3.54 4.16
MLTA 18.63 21.37 0.18 18.45 21.04 23.83 18.53
MLATA 13.0 14.55 11.25 -2.24 0.02 -2.96 15.04
LstarB 3.87 3.84 5.54 3.55 3.81 5.59 3.64
MLTB 0.28 18.74 21.27 24.0 18.29 20.99 23.83
MLATB 14.82 5.82 7.11 3.98 1.52 4.48 2.19

Figure 2.

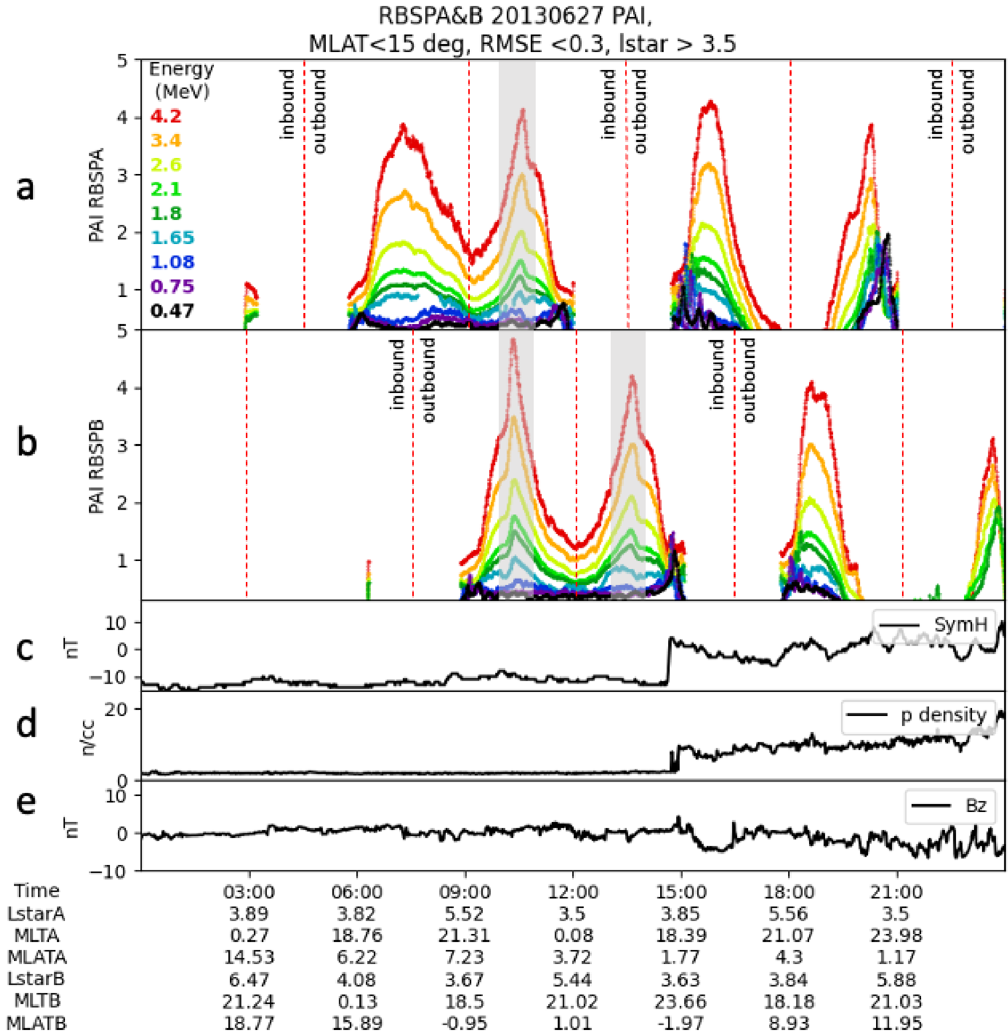
RBSPA&B 20130627 PAI,
MLAT<15 deg, RMSE <0.3, lstar > 3.5
Energy (MeV)
4.2
3.4
2.6
2.1
1.8
1.65
1.08
0.75
0.47
inbound
outbound
a
b
c
d
e
PAI RBSPA
PAI RBSPB
SymH
p density
Bz
nT
n/cc
Time 03:00 06:00 09:00 12:00 15:00 18:00 21:00
LstarA 3.89 3.82 5.52 3.5 3.85 5.56 3.5
MLTA 0.27 18.76 21.31 0.08 18.39 21.07 23.98
MLATA 14.53 6.22 7.23 3.72 1.77 4.3 1.17
LstarB 6.47 4.08 3.67 5.44 3.63 3.84 5.88
MLTB 21.24 0.13 18.5 21.02 23.66 18.18 21.03
MLATB 18.77 15.89 -0.95 1.01 -1.97 8.93 11.95

Figure 3.

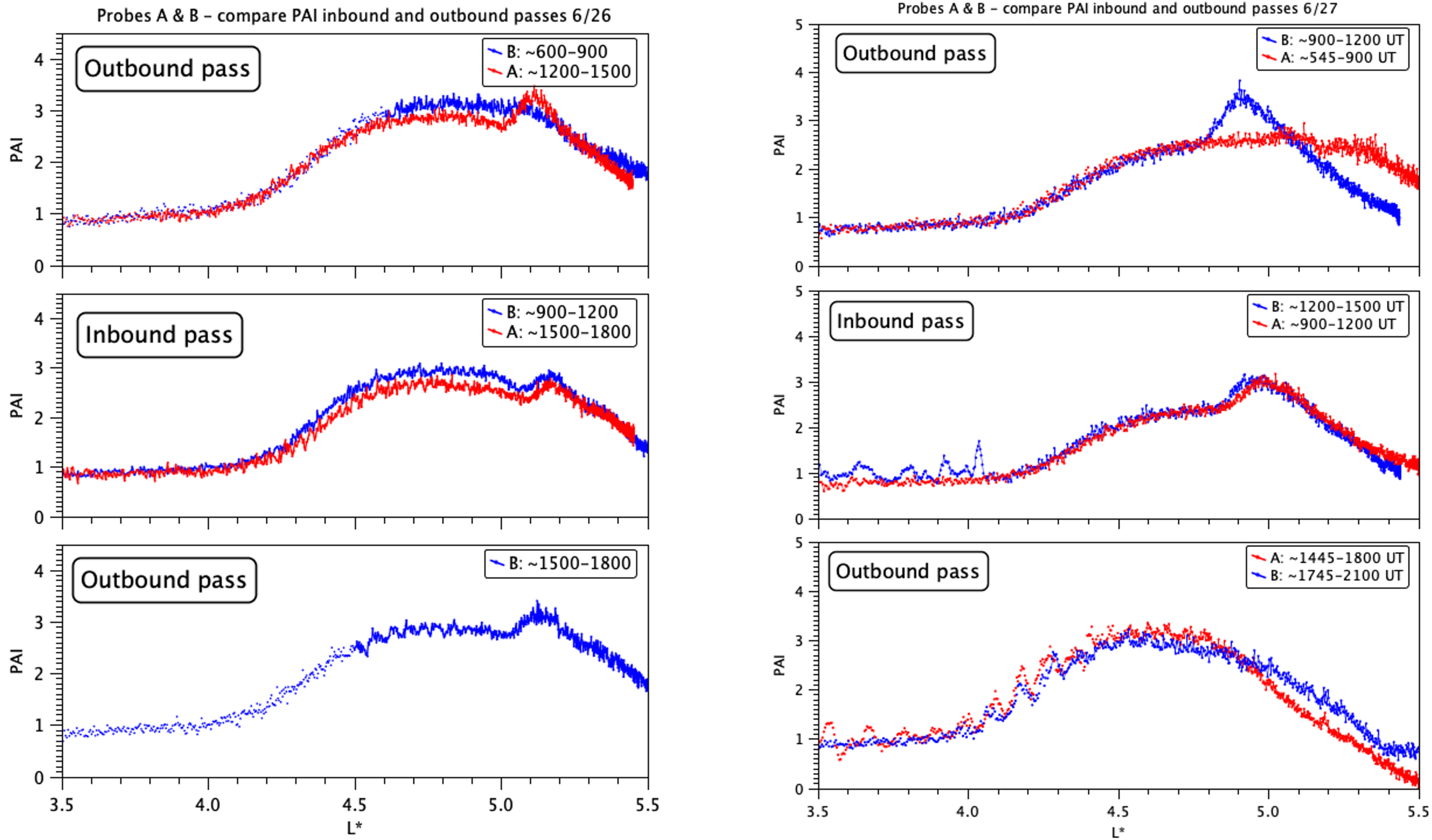
Probes A & B - compare PAI inbound and outbound passes 6/26
Outbound pass
B: ~600-900
A: ~1200-1500
Inbound pass
B: ~900-1200
A: ~1500-1800
Outbound pass
B: ~1500-1800
PAI
L*
Probes A & B - compare PAI inbound and outbound passes 6/27
Outbound pass
B: ~900-1200 UT
A: ~545-900 UT
Inbound pass
B: ~1200-1500 UT
A: ~900-1200 UT
Outbound pass
A: ~1445-1800 UT
B: ~1745-2100 UT

Figure 4.

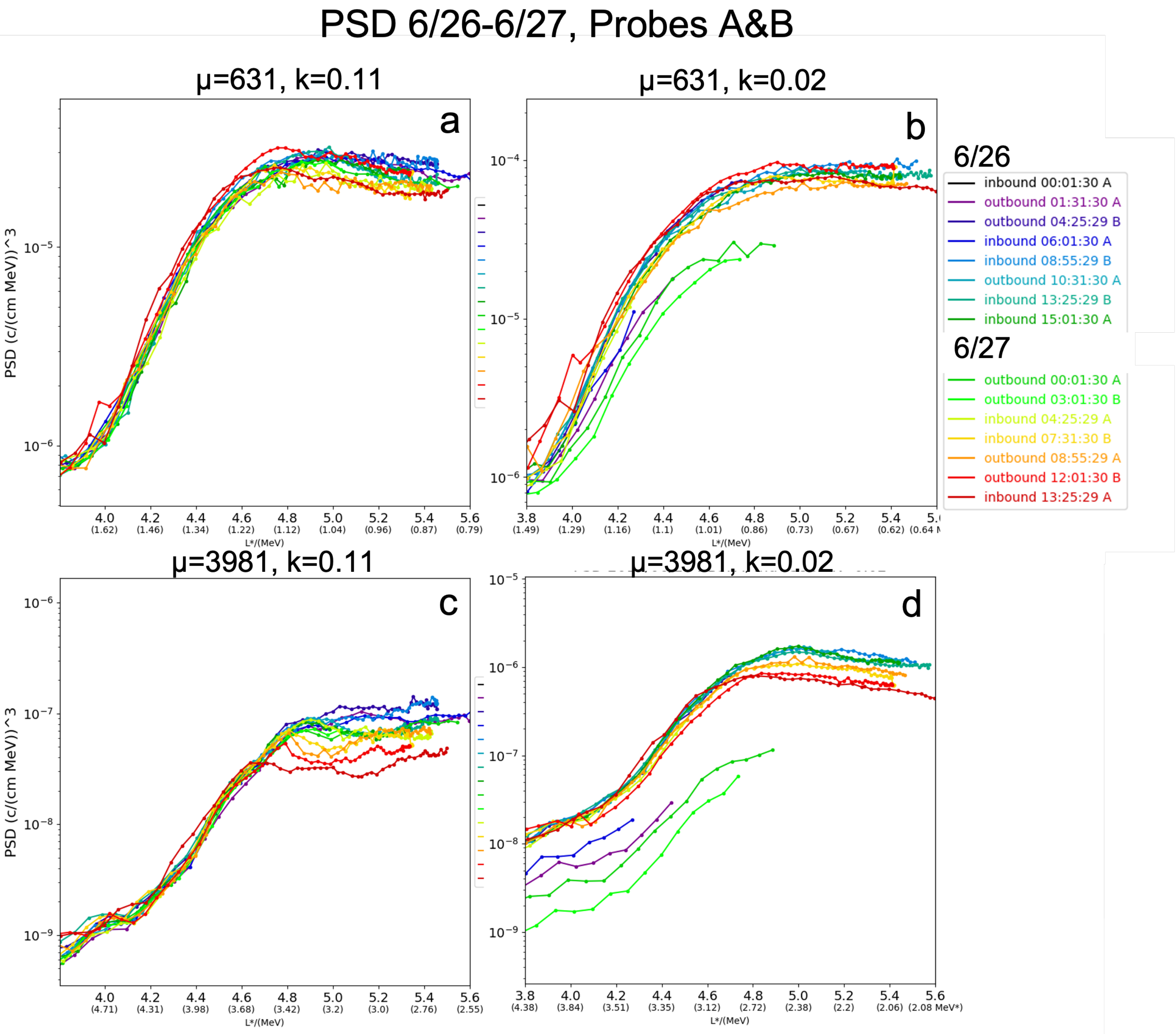
PSD 6/26-6/27, Probes A&B
μ=631, k=0.11
a
μ=631, k=0.02
b
μ=3981, k=0.11
c
μ=3981, k=0.02
d
PSD (c/(cm MeV))^3
L*/(MeV)
6/26
inbound 00:01:30 A
outbound 01:31:30 A
outbound 04:25:29 B
inbound 06:01:30 A
inbound 08:55:29 B
outbound 10:31:30 A
inbound 13:25:29 B
inbound 15:01:30 A
6/27
outbound 00:01:30 A
outbound 03:01:30 B
inbound 04:25:29 A
inbound 07:31:30 B
outbound 08:55:29 A
outbound 12:01:30 B
inbound 13:25:29 A

Figure 5.

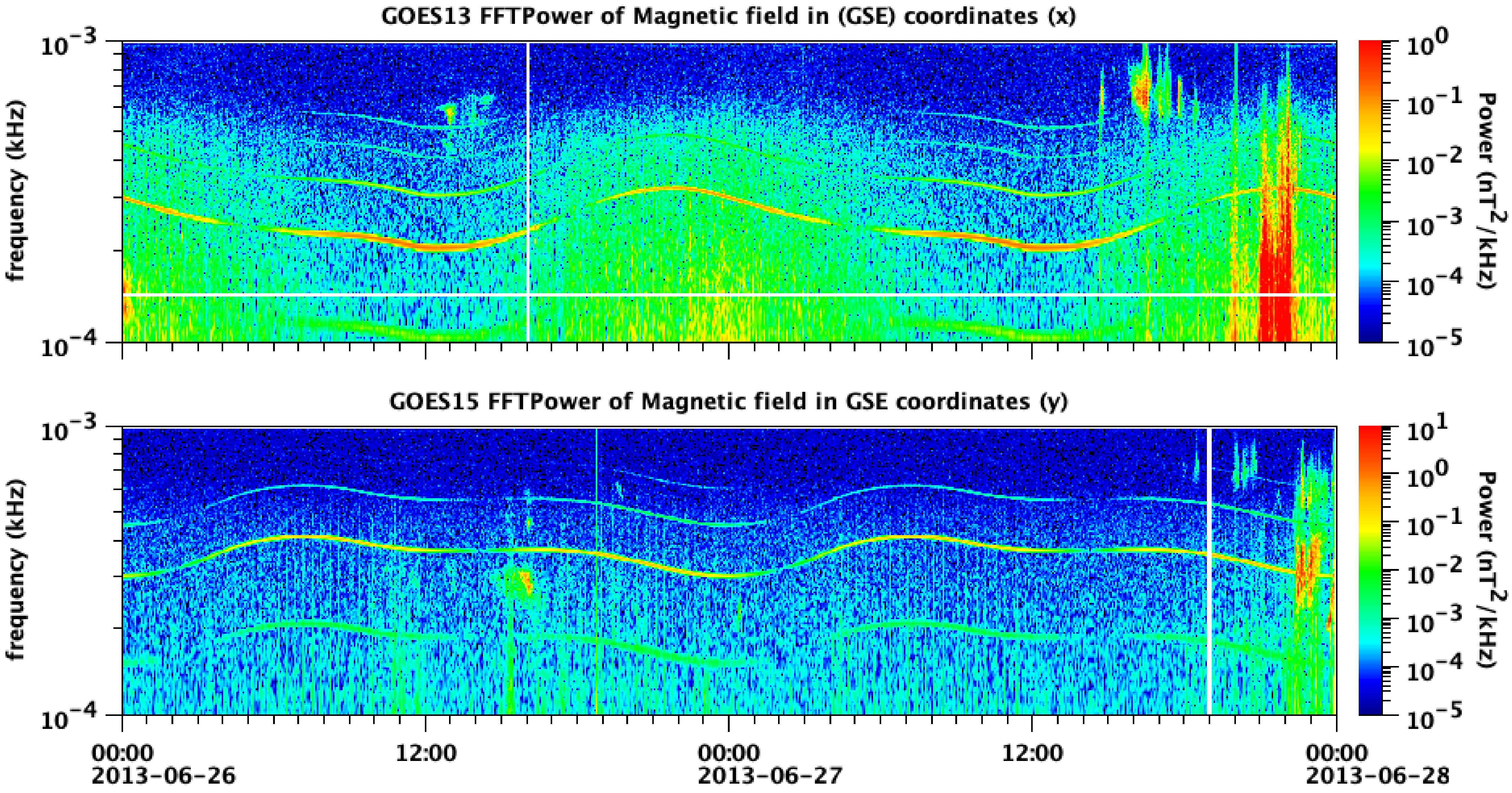

GOES13 FFTPower of Magnetic field in (GSE) coordinates (x)
frequency (kHz)
Power (nT²/kHz)
GOES15 FFTPower of Magnetic field in GSE coordinates (y)
frequency (kHz)
Power (nT²/kHz)
00:00
2013-06-26
12:00
00:00
2013-06-27
12:00
00:00
2013-06-28

Figure 6.

L-shell
Carisma FFT spectrograms
7.85
YKC kHz
7.16
FCC kHz
6.64
FSMI kHz
5.03
LARG kHz
4.83
TPAS kHz
4.13
MSTK kHz
nT^2/kHz
00:00
2013-06-26
12:00
00:00
2013-06-27
12:00
00:00
2013-06-28
L-shell
SGO FFT Spectrograms
6.2
KIL kHz
5.9
IVA kHz
5.4
SOD kHz
5.2
OUL kHz
arb. units
00:00
2013-06-26
12:00
00:00
2013-06-27
12:00
00:00
2013-06-28

Figure 7.

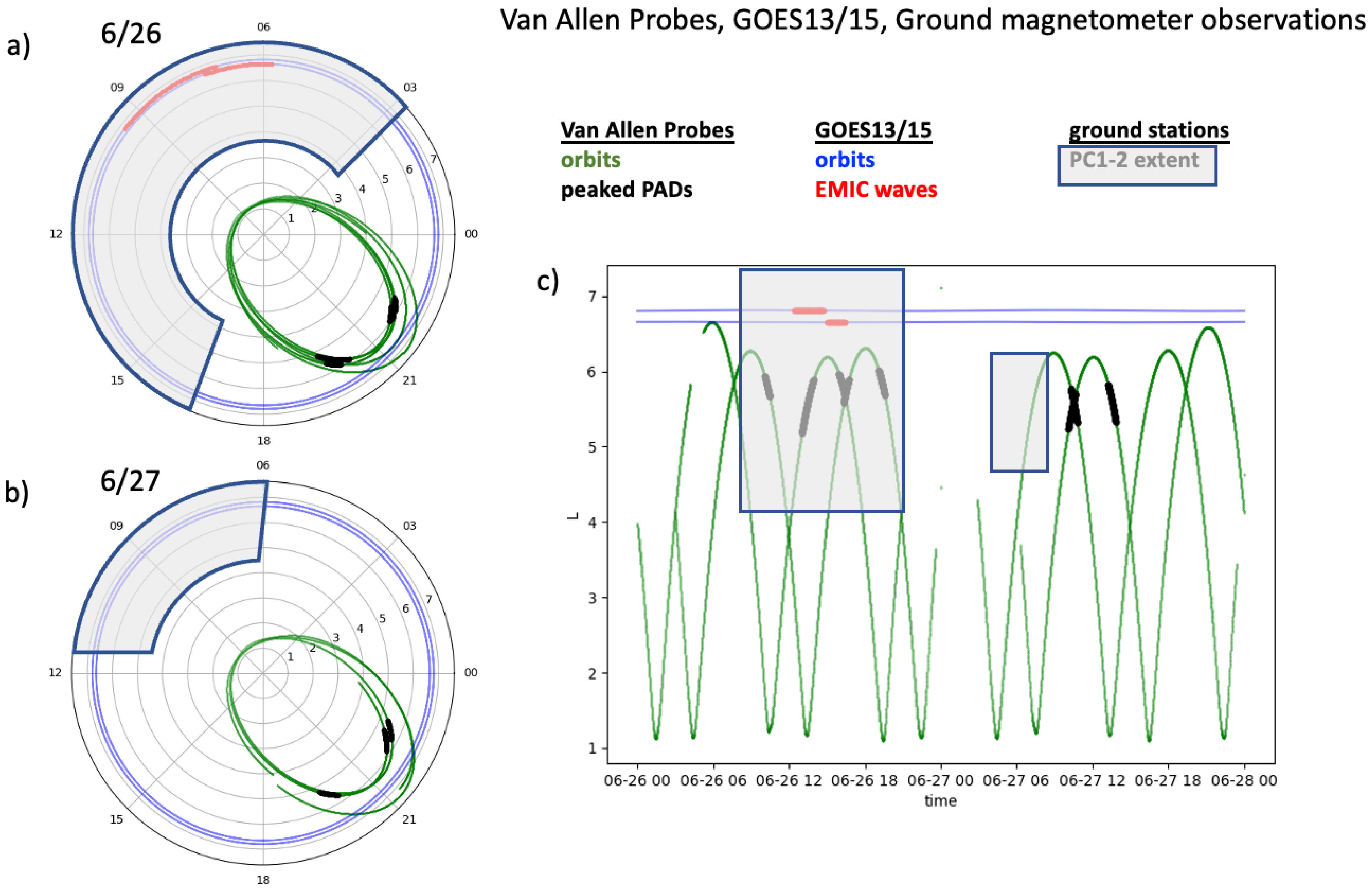
Van Allen Probes, GOES13/15, Ground magnetometer observations
a)
6/26
b)
6/27
c)
Van Allen Probes
orbits
peaked PADs
GOES13/15
orbits
EMIC waves
ground stations
PC1-2 extent
06
03
00
21
18
15
12
09
1
2
3
4
5
6
7
L
time
06-26 00
06-26 06
06-26 12
06-26 18
06-27 00
06-27 06
06-27 12
06-27 18
06-28 00